Attenuation correction of *L*-shell X-ray fluorescence computed tomography imaging *

LIU Long(刘珑)[1,2] HUANG Yang(黄旸)[1,2] XU Qing(徐清)[1] YAN Ling-Tong(闫灵通)[1]
LI Li(李丽)[1] FENG Song-Lin(冯松林)[1] FENG Xiang-Qian(冯向前)[1;1)]

[1] Key Laboratory of Nuclear Radiation and Nuclear Energy Technology, Institute of High Energy Physics, Chinese Academy of Sciences, Beijing 100049, China
[2] University of Chinese Academy of Sciences, Beijing 100049, China

Abstract: X-ray Fluorescence Computed Tomography (XFCT) is a widely-used experimental technique for investigating the spatial distribution of elements in a sample. However, image reconstruction for this technique is more difficult than for transmission tomography, one problem being self-absorption. In this work, we make use of known quantities and unknown density of elements of interest to express unknown attenuation maps. The attenuation maps are added to the contribution value of the pixel in the Maximum Likelihood Expectation Maximization (MLEM) reconstruction method. Results indicate that the relative error is less than 14.1%, which shows that this method can effectively correct L-shell XFCT.

Key words: attenuation correction, *L*-shell, XFCT

PACS: 29.30.Kv, 07.85. **DOI:** 10.1088/1674-1137/39/3/038203

1 Introduction

X-ray Fluorescence Computed Tomography (XFCT) is an experimental technique which can reconstruct the distribution of elements within a sample by measuring fluorescence stimulated from the sample [1]. The sample is irradiated with an X-ray beam, of energy greater than the K-shell or L-shell energy of the elements of interest, which stimulates fluorescence in the sample atoms. An energy-discriminating detector is placed at a 90-degree angle to the X-ray beam direction to detect and compensate for attenuation of fluorescence due to Compton scattering [2]. Each element has its own characteristic fluorescence, and the intensity of that fluorescence indicates the quantity of that element in a sample. The distribution of a particular element in a sample can be reconstructed using fluorescence measurements when the sample is scanned and rotated, if attenuation can be neglected [3]. To reconstruct a more accurate element distribution image, attenuation correction is necessary [4, 5]. Hogan et al. present a method using Filtered Back Projection (FBP) with attenuation correction in the XFCT reconstruction, in which the attenuation coefficient distribution at incident energy and fluorescence energy must be known [6]. Golosio et al. give a method that solves the attenuation problem by combining X-ray fluorescence, Compton and transmission tomography [7].

La Riviere and Billmire have developed an alternating-update iterative reconstruction algorithm based on maximizing a penalized Poisson likelihood objective function [8]. In their work, the unknown linear attenuation coefficients at fluorescence energy are expressed as a linear combination of known attenuation coefficients at the incident energy and the unknown concentration of the element. However, this absorption method only applies to two energy regions: that above the K-edge energy and that between K-edge energy and L_1-edge energy. Magdalena Bazalova et al. have done research on a method of getting the Pt distribution of Cisplatin with K-shell and L-shell XFCT [9]. In their research, they find that the sensitivity of K-shell XFCT with 80 keV X-rays is 4.4 and 3.0 times lower than that of L-shell XFCT with a 15 keV excitation beam for 2 cm and 4 cm diameter phantoms respectively. The Cisplatin concentration error decreases from 63% to 12% when attenuation correction is incorporated in the L-shell XFCT iterative reconstruction algorithm. However, few studies focus on attenuation correction for L-shell XFCT.

In the present work, the energy region above $M1$-edge energy is considered. The attenuation coefficient at the incident energy can be expressed as a linear combination of $E^{-2.83}$ and $E^{-2.6628}$ because the incident energy in our

Received 28 April 2014, Revised 16 August 2014
∗ Supported by National Natural Science Foundation of China (11205167, 11305183, 11175190)
1) Corresponding author. E-mail: fengxq@ihep.ac.cn

experiment is between the L_1-edge energy and K-edge energy of Ba, and above the K-edge energy of other elements. It can be obtained using the dual-energy method [10]. The unknown attenuation coefficient can then be expressed as a function of the unknown density ρ of the element. After that, the attenuation coefficients are added to the contribution value of each pixel in the Maximum Likelihood Expectation Maximization (MLEM) reconstruction method. We aim to test the feasibility of this method, and it is hoped that the attenuation correction of L-shell XFCT will be resolved with our proposed method.

2 Method

2.1 Unknown attenuation maps

In order to obtain the unknown fluorescence maps at the energy $E_{K_\alpha}^{(n)}$ or $E_{L_1}^{(n)}$ of the element n of interest, the mass attenuation coefficient for a given element can be shown as (1) [11]:

$$\left(\frac{\mu}{\rho}\right)^{(n)}(E)=C^{(n)}(E)E^{-\gamma^{(n)}(E)}. \tag{1}$$

Both $C^{(n)}(E)$ and $\gamma^{(n)}(E)$ are functions of energy but they change only when crossing absorption edges. In XFCT, two energy regions are of interest for low-Z elements: the region above the K-edge energy $E_K^{(n)}$, and the region between the K-edge energy $E_K^{(n)}$ and L_1-edge energy $E_{L_1}^{(n)}$. For high-Z elements, four energy regions are of interest: between K-edge energy $E_K^{(n)}$ and L_1-edge energy $E_{L_1}^{(n)}$; between L_1-edge energy $E_{L_1}^{(n)}$ and L_2-edge energy $E_{L_2}^{(n)}$; between L_2-edge energy $E_{L_2}^{(n)}$ and L_3-edge energy $E_{L_3}^{(n)}$; and between L_3-edge energy $E_{L_3}^{(n)}$ and M_1-edge energy $E_{M_1}^{(n)}$.

$C^{(n)}(E)$ and $\gamma^{(n)}(E)$ can be shown as [11]:

$$C^{(n)}(E)=\begin{cases} C_1 E>E_{K_\alpha} \\ C_2 E_{K_\alpha}>E>E_{L_1} \\ C_3 E_{L_1}>E>E_{L_2} \\ C_4 E_{L_2}>E>E_{L_3} \\ C_5 E_{L_3}>E>E_{M_1} \end{cases}, \tag{2}$$

where C_1, C_2, C_3, C_4 and C_5 are element-specific.

$$\gamma^{(n)}(E)=\begin{cases} 2.83 E>E_{K_\alpha} \\ 2.6628 E_{K_\alpha}>E>E_{L_1} \\ 2.6865 E_{L_1}>E>E_{L_2} \\ 2.5825 E_{L_2}>E>E_{L_3} \\ 2.5065 E_{L_3}>E>E_{M_1} \end{cases}. \tag{3}$$

Consider a mixture of N elements, which consist of N_1 elements whose K-edge energy is lower than the incident energy and N_2 elements whose K-edge energy is higher than the incident energy and L_1-edge energy is lower than the incident energy. The linear attenuation coefficient at energy E can be written

$$\mu(E) = \sum_1^{N_1} C_1^{(n_1)}(E)E^{-2.83}\rho^{(n_1)} + \sum_1^{N_2} C_2^{(n_2)}(E)E^{-2.6628}\rho^{(n_2)}, \tag{4}$$

which can be rewritten as

$$\mu(E) = \left(\sum_1^{N_1} C_1^{(n)}(E)\rho^{(n_1)}\right)E^{-2.83} + \left(\sum_1^{N_2} C_2^{(n)}(E)\rho^{(n_2)}\right)E^{-2.6628}. \tag{5}$$

If the K-edge energy of the highest-Z element N is lower than the incident X-ray energy, the linear attenuation coefficient at energy $E_{K_\alpha}^{(N_1)}$ can be written as

$$\begin{aligned}\mu\left(E_{K_\alpha}^{(N_1)}\right) = &\left(\sum_1^{N_1} C_1^{(n)}(E_{\rm I})\rho^{(n_1)}\right)\left(E_{K_\alpha}^{(N_1)}\right)^{-2.83} \\ &+\left(\sum_1^{N2} C_2^{(n)}(E_{\rm I})\rho^{(n_2)}\right)\left(E_{K_\alpha}^{(N_1)}\right)^{-2.6628} \\ &+\left(\left(E_{K_\alpha}^{(N_1)}\right)^{-2.6628} C_2^{(N_1)} \right. \\ &\left.-\left(E_{K_\alpha}^{(N_1)}\right)^{-2.83} C_1^{(N_1)}\right)\rho^{(N_1)}.\end{aligned} \tag{6}$$

If the incident X-ray energy is between the L_1-edge and K-edge energies of the highest-Z element N, the linear attenuation coefficient at energy $E_{L_1}^{(N_2)}$ can be written

$$\begin{aligned}\mu\left(E_{L_1}^{(N_2)}\right) = &\left(\sum_1^{N_1} C_1^{(n)}(E_{\rm I})\rho^{(n_1)}\right)\left(E_{L_1}^{(N_2)}\right)^{-2.83} \\ &+\left(\sum_1^{N_2} C_2^{(n)}(E_{\rm I})\rho^{(n_2)}\right)\left(E_{L_1}^{(N_2)}\right)^{-2.6628} \\ &+\left(\left(E_{L_1}^{(N_2)}\right)^{-2.5065} C_3^{(N_2)} \right. \\ &\left.-\left(E_{L_1}^{(N_2)}\right)^{-2.6628} C_2^{(N_2)}\right)\rho^{(N_2)}.\end{aligned} \tag{7}$$

The unknown attenuation coefficients $\mu\left(E_{K_\alpha}^{(N_1)}\right)$ at energy E_{K_α} of element N_1 and $\mu\left(E_{L_1}^{(N_2)}\right)$ at energy E_{L_1} of element N_2 can therefore be expressed as a function involving the known attenuation coefficient $\mu(E_{\rm I})$ and the unknown density ρ. Thus the question of image construction can be translated to the construction of the element concentration.

After crossing the absorption edge of the highest-Z

element, the reconstruction of the lower-Z elements is possible with the density maps and attenuation maps of the higher-Z elements. The attenuation coefficients of element n_1, of which the K-edge energy is lower than the incident beam energy, and element n_2, of which the K-edge energy is higher than the incident beam energy, can be expressed by (8) and (9).

$$\begin{aligned}\mu\left(E_{K\alpha}^{(n_1)}\right) = &\left(\sum_1^{N_1} C_1^{(n)}(E_{\rm I})\rho^{(n_1)}\right)\left(E_{K\alpha}^{(n_1)}\right)^{-2.83}\\ &+\left(\sum_1^{N_2} C_2^{(n)}(E_{\rm I})\rho^{(n_2)}\right)\left(E_{K\alpha}^{(n_1)}\right)^{-2.6628}\\ &+\sum_{n_1+1}^{N_1}\left(\left(E_{K\alpha}^{(n_1)}\right)^{-2.6628}C_2^{(i1)}\right.\\ &\left.-\left(E_{K\alpha}^{(n_1)}\right)^{-2.83}C_1^{(i1)}\right)\rho^{(i1)}\\ &+\sum_{n_2+1}^{N_2}\left(\left(E_{K\alpha}^{(n_1)}\right)^{-2.5065}C_3^{(i2)}\right.\\ &\left.-\left(E_{K\alpha}^{(n_1)}\right)^{-2.6628}C_2^{(i2)}\right)\rho^{(i2)}\\ &+\left(\left(E_{K\alpha}^{(n_1)}\right)^{-2.6628}C_2^{(n_1)}\right.\\ &\left.-\left(E_{K\alpha}^{(n_1)}\right)^{-2.83}C_1^{(n_1)}\right)\rho^{(n_1)}. \qquad (8)\end{aligned}$$

$$\begin{aligned}\mu\left(E_{L_1}^{(n_2)}\right) = &\left(\sum_1^{N_1} C_1^{(n)}(E_{\rm I})\rho^{(n_1)}\right)\left(E_{L_1}^{(n_2)}\right)^{-2.83}\\ &+\left(\sum_1^{N_2} C_2^{(n)}(E_{\rm I})\rho^{(n_2)}\right)\left(E_{L_1}^{(n_2)}\right)^{-2.6628}\\ &+\sum_{n_1+1}^{N_1}\left(\left(E_{L_1}^{(n_2)}\right)^{-2.6628}C_2^{(i1)}\right.\\ &\left.-\left(E_{L_1}^{(n_2)}\right)^{-2.83}C_1^{(i1)}\right)\rho^{(i1)}\\ &+\sum_{n_2+1}^{N_2}\left(\left(E_{L_1}^{(n_2)}\right)^{-2.5065}C_3^{(i2)}\right.\\ &\left.-\left(E_{L_1}^{(n_2)}\right)^{-2.6628}C_2^{(i2)}\right)\rho^{(i2)}\\ &+\left(\left(E_{L_1}^{(n_2)}\right)^{-2.5065}C_3^{(n_2)}\right.\\ &\left.-\left(E_{L_1}^{(n_2)}\right)^{-2.6628}C_2^{(n_2)}\right)\rho^{(n_2)}. \qquad (9)\end{aligned}$$

2.2 MLEM image reconstruction

Image reconstruction methods include analytical methods and iterative methods. A typical analytical method is FBP, while a typical iterative method is MLEM [12]. The main advantage of the FBP method is the fast reconstruction speed, while the main disadvantage is its poor noise suppression. The MLEM method, on the other hand, has slower reconstruction speed but better noise suppression. The MLEM algorithm can be expressed as (10) [13]:

$$\begin{aligned}f^{(p+1)}(i,j) = &\frac{f^{(p)}(i,j)}{\sum\limits_{m,n}k(i,j,m,n)}\\ &\times\sum_{m,n}\frac{K(i,j,m,n)I(m,n)}{\sum\limits_{ii,jj}K(ii,jj,m,n)f^{(p)}(ii,jj)}, \qquad (10)\end{aligned}$$

where $f^{(p)}(i,j)$ is the estimated element density after iterating p times and $I(m,\ n)$ represents the projection value. $K(i,\ j,\ m,\ n)$ denotes the contribution of pixel (i, j) to $I(m,\ n)$:

$$K(i,j,m,n)=K'(i,j,m,n)f(\theta,s,t)g(\theta,s,t), \qquad (11)$$

where K' $(i,\ j,\ m,\ n)$ is the weighting function without regard to the self-absorption effect. $f(\theta,s,t)$ represents the attenuation of the beam intensity when transmitting to the stimulated point of the sample:

$$f(\theta,s,t)=\exp\left(-\int_{-\infty}^{s}\mu(s',t,E_{\rm I})\mathrm{d}s'\right). \qquad (12)$$

$g(\theta,s,t)$ is the fluorescence attenuation ratio when transmitting from the stimulated point of the sample to the detector:

$$g(\theta,s,t)=\int_{\Omega_0}^{\Omega_1}\exp\left(-\int_0^L\mu(s,t,E_{\rm f})\mathrm{d}l\right)\mathrm{d}\Omega. \qquad (13)$$

2.3 Geant4 simulation

Geant4 is a toolkit to simulate the passage of particles through matter [14, 15]. A large number of experiments and projects use it in a variety of application domains, such as high energy physics, astrophysics and space science, medical physics and radiation protection. The geometry of the system, the primary particles and the physical processes undergone by the particles must all be defined to simulate a system. Geant4 provides many physical models such as standard electromagnetic models, low energy electromagnetic models, and so on. The standard electromagnetic models are suitable for most of the Geant4 simulations involving electromagnetic processes, except for low energy particles [16]. Livermore and Penelop are the low energy electromagnetic models used to simulate processes involving low energy particles. The Low Energy Electromagnetic package provides all kinds of models describing the electromagnetic processes of electrons and positrons, photons, charged hadrons and ions with an eye to detailed features, such as atomic shell effects and charge dependence [17].

Our XFCT system was simulated with Geant4, with

the geometry of the simulation system as shown in Fig. 1. The X-ray tube is on the far left, with a Be-filter to its right, in the beam direction. The sample is in the middle, and has the composition shown in Table 1. Above the sample is an energy dispersion detector and to the right of the sample is another detector. The system is placed in a vacuum, to avoid attenuation due to air. In the simulation system, there are two models for the X-ray source. One model is a monochromatic X-ray, which is used to simulate synchrotron radiation light. The other is a polychrome X-ray, which simulates an X-ray tube.

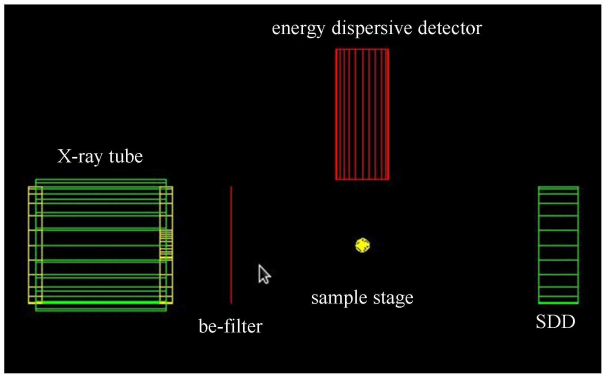

Fig. 1. Geometry of the XFCT Geant4 simulation.

Table 1. Chemical composition of cylindrical sample.

phase index	density/(g/cm^3)	oxides	content (wt%)
1	2.2	SiO_2	100
2	2.4	SiO_2	51
		CaO	20
		Fe_2O_3	15
		BaO	14

To test the accuracy of the attenuation correction method, a simulation experiment was performed using a cylindrical sample with the chemical composition described in Table 1. As shown in Fig. 2, the sample was composed of a cylindrical tube with an inner diameter of 0.02 mm and an external diameter of 0.04 mm, enclosing a cylinder of diameter 0.02 mm. During the experiment, the sample was rotated through 180 degrees in 5-degree steps. The number of scanning beams was 81, and the scanning region was between −0.05 mm and +0.05 mm with respect to the centre of the sample. The energy dispersion detector was used to detect the fluorescence through the attenuation of the sample at each projection. The data was stored in a two-dimensional matrix, in which the first dimension was the number of the X-ray beam and the second dimension was the energy of the ray.

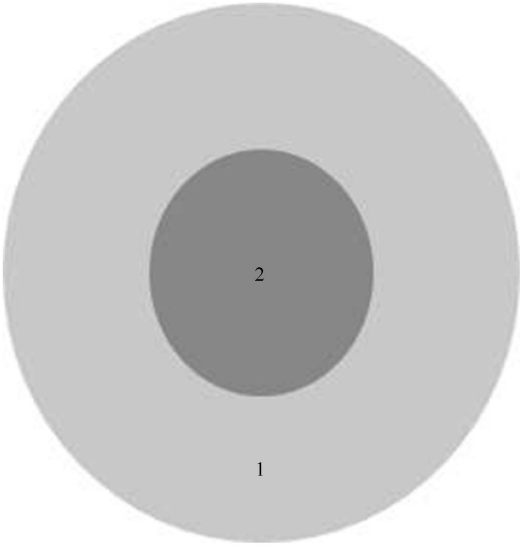

Fig. 2. Cross-section of the cylindrical sample, with 1 and 2 indicating the material phase index as given in Table 1.

3 Results and discussion

Geant4-simulated XFCT images for the sample above, reconstructed with FBP and MLEM with and without attenuation correction, are shown in Fig. 3. The XFCT images reconstructed with FBP are much noisier but sharper than those with MLEM without attenuation correction, which shows that noise suppression with FBP is less than with MLEM. The time consumed for MLEM was much longer than that for FBP, however. For 40×40 pixels, the time consumed for image reconstruction with 10 MLEM iterations without attenuation correction was about 20 minutes, while the time consumed for image reconstruction with FBP was less than 1 minute.

True and estimated Fe density and Ba density are shown in Tables 2 and 3. In the XFCT images, Fe densities in the bottom nine pixels (called the bottom object) and the central nine pixels (called the central object) were underestimated by 78.2% and 69.8%respectively with FBP, and 24.6% and 54.5% respectively in MLEM without attenuation correction. After attenuation correction, Fe densities were within 6.3% of true values. Attenuation played a more important role in Ba density image reconstruction. Bottom object Ba densities were underestimated by 90.5% and 76.3% in FBP and MLEM without attenuation correction. Using MLEM with attenuation correction, measured Ba density was within 14.1% of the true value.

Bazalova et al. [9] researched a method of getting Pt distribution in Cisplatin, and found that the sensitivity of the K-shell XFCT was lower than that of L-shell

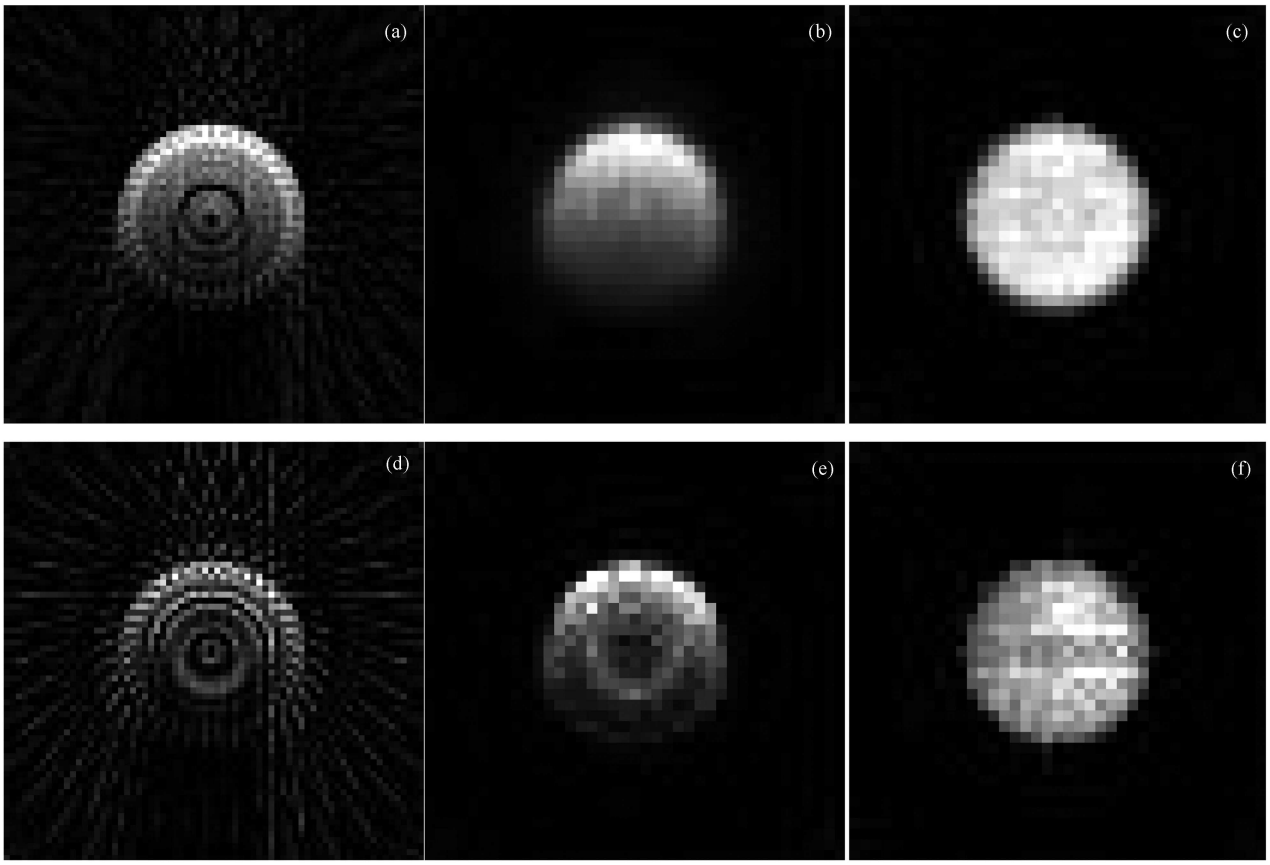

Fig. 3. Reconstruction images of Fe distribution and Ba distribution. (a) Fe distribution with FBP; (b) Fe distribution with MLEM without attenuation; (c) Fe distribution with MLEM with attenuation; (d) Ba distribution with FBP; (e) Ba distribution with MLEM without attenuation; (f) Ba distribution with MLEM with attenuation.

Table 2. True and estimated Fe density.

method	location	true value/(g/cm^3)	estimated value/(g/cm^3)	difference (%)
FBP	bottom object	0.252	0.055	78.2
	central object	0.252	0.076	69.8
MLEM without attenuation	bottom object	0.252	0.190	24.6
	central object	0.252	0.115	54.4
MLEM with attenuation	bottom object	0.252	0.255	1.2
	central object	0.252	0.236	6.3

Table 3. True and estimated Ba density.

method	location	true value/(g/cm^3)	estimated value/(g/cm^3)	difference (%)
FBP	bottom object	0.304	0.029	90.5
	central object	0.304	0.035	88.5
MLEM without attenuation	bottom object	0.304	0.072	76.3
	central object	0.304	0.034	88.8
MLEM with attenuation	bottom object	0.304	0.267	12.2
	central object	0.304	0.261	14.1

XFCT. Since then, however, little has appeared in the literature about L-shell attenuation correction. We have presented an attenuation correction method for L-shell XFCT. The relative error decreased from 88.8% to 14.1% after attenuation correction in Ba density reconstruction. This method can be used to reconstruct L-shell XFCT images of biological samples. A drawback of this method is that samples are irradiated by two different X-rays, which will increase the radiation dose of samples. Another point is that this study simulated an XFCT system using monoenergetic beams, which greatly reduced the complexity in attenuation. Besides, for a real XFCT system, an array of crystals with individual readout channels, as is used for many CT systems, is more practical for experimental XFCT.

4 Conclusion

Unknown attenuation maps are expressed by the known quantities and the unknown density of an element of interest in the attenuation correction of L-shell XFCT, which has been proved feasible by Geant4 simulation. Results indicate that this method can significantly increase accuracy of the reconstructed XFCT image. This method may have even more application in XFCT attenuation correction for large biological samples.

References

1 Simionovici A, Chukalina M, Schroer C et al. IEEE Transaction on Nuclear Science, 2000, **47**(6): 2736–2740
2 CONG W, SHEN H, CAO G et al. J X-ray Sci. Technol., 2013, **21**(1): 1–8
3 Schroer C G. Applied Physics Letters, 2001, **79**(12): 1912
4 Kim K S, YE J C. Phys. Med. Biol., 2011, **56**(15): 4991–5009
5 Martinez-Moller A, Nekolla S G. Med. Phys., 2012, **22**(4): 299–310
6 Hogan J P, Gonsalves R A, Krieger A S. IEEE Transaction on Nuclear Science, 1991, **38**(6): 1721–1727
7 Golosio B, Simionovici A, Somogyi A et al. Journal of Applied Physics, 2003, **94**(1): 145
8 La Riviere P J, Billmire D M. Proc. of SPIE, 2004, **5535**: 243–252
9 Bazalova M, Ahmad M, Pratx G et al. Phys. Med. Biol., 2014, **59**(1): 219–232
10 Noh J, Fessler J A, Kinahan P E. IEEE Transaction on Medical Imaging, 2009, **28**(11): 1688–1701
11 Leroux J. Advances in X-ray Analysis, 1962, **5**: 153–160
12 Wieczorek H. Phys. Med. Biol., 2010, **55**(11): 3161–3176
13 Hebert T J, Leahy R. IEEE Transaction on Nuclear Science, 1990, **37**(2): 754–758
14 Agostinelli S, Allison J, Amako K et al. Nuclear Instruments and Methods in Physics Research Section A: Accelerators, Spectrometers, Detectors and Associated Equipment, 2003, **506**(3): 250–303
15 Allison K A J, Apostolakis J, Araujo H et al. IEEE Transaction on Nuclear Science, 2006, **52**(1): 270–278
16 Kadri O, Ivanchenko V N, Gharbi F et al. Nuclear Instruments and Methods in Physics Research Section B: Beam Interactions with Materials and Atoms, 2007, **258**(2): 381–387
17 Chauvie S, Guatelli S, Ivanchenko V et al. IEEE Nuclear Science Symposium Conference Record, 2004, **3**: 1881–1885